

High-precision photometry by telescope defocussing. VIII. WASP-22, WASP-41, WASP-42 and WASP-55*

John Southworth¹, J. Tregloan-Reed², M. I. Andersen³, S. Calchi Novati^{4,5,6}, S. Ciceri⁷,
J. P. Colque⁸, G. D’Ago⁶, M. Dominik^{9†}, D. F. Evans¹, S.-H. Gu^{10,11}, A. Herrera-Cordova⁸,
T. C. Hinse¹², U. G. Jørgensen¹³, D. Juncher¹³, M. Kuffmeier¹³, L. Mancini^{7,14},
N. Peixinho⁸, A. Popovas¹³, M. Rabus^{15,7}, J. Skottfelt^{16,13}, R. Tronsgaard¹⁷,
E. Unda-Sanzana⁸, X.-B. Wang^{10,11}, O. Wertz¹⁸, K. A. Alsubai¹⁹, J. M. Andersen^{13,20},
V. Bozza^{5,21}, D. M. Bramich¹⁹, M. Burgdorf²², Y. Damerdji¹⁸, C. Diehl^{23,24},
A. Elyiv^{25,18,26}, R. Figuera Jaimes^{9,27}, T. Haugbølle¹³, M. Hundertmark¹³, N. Kains²⁸,
E. Kerins²⁹, H. Korhonen^{30,13,3}, C. Liebig⁹, M. Mathiasen¹³, M. T. Penny³¹, S. Rahvar³²,
G. Scarpetta^{6,5,21}, R. W. Schmidt²³, C. Snodgrass³³, D. Starkey⁹, J. Surdej¹⁸, C. Vilela¹,
C. von Essen¹⁷, Y. Wang¹⁰

¹ Astrophysics Group, Keele University, Staffordshire, ST5 5BG, UK

² NASA Ames Research Center, Moffett Field, CA 94035, USA

³ Dark Cosmology Centre, Niels Bohr Institute, University of Copenhagen, Juliane Maries vej 30, 2100 Copenhagen Ø, Denmark

⁴ NASA Exoplanet Science Institute, MS 100-22, California Institute of Technology, Pasadena, CA 91125, US

⁵ Dipartimento di Fisica “E.R. Caianiello”, Università di Salerno, Via Giovanni Paolo II 132, 84084, Fisciano (SA), Italy

⁶ Istituto Internazionale per gli Alti Studi Scientifici (IIASS), 84019 Vietri Sul Mare (SA), Italy

⁷ Max Planck Institute for Astronomy, Königstuhl 17, 69117 Heidelberg, Germany

⁸ Unidad de Astronomía, Facultad de Ciencias Básicas, Universidad de Antofagasta, Avenida U. de Antofagasta 02800, Antofagasta, Chile

⁹ SUPA, University of St Andrews, School of Physics & Astronomy, North Haugh, St Andrews, KY16 9SS, UK

¹⁰ Yunnan Observatories, Chinese Academy of Sciences, Kunming 650011, China

¹¹ Key Laboratory for the Structure and Evolution of Celestial Objects, Chinese Academy of Sciences, Kunming 650011, China

¹² Korea Astronomy and Space Science Institute, Daejeon 305-348, Republic of Korea

¹³ Niels Bohr Institute & Centre for Star and Planet Formation, University of Copenhagen, Øster Voldgade 5, 1350 Copenhagen K, Denmark

¹⁴ INAF – Osservatorio Astrofisico di Torino, via Osservatorio 20, 10025, Pino Torinese, Italy

¹⁵ Instituto de Astrofísica, Facultad de Física, Pontificia Universidad Católica de Chile, Av. Vicuña Mackenna 4860, 7820436 Macul, Santiago, Chile

¹⁶ Centre of Electronic Imaging, Department of Physical Sciences, The Open University, Milton Keynes, MK7 6AA, UK

¹⁷ Stellar Astrophysics Centre (SAC), Department of Physics and Astronomy, Aarhus University, Ny Munkegade 120, DK-8000 Aarhus C, Denmark

¹⁸ Institut d’Astrophysique et de Géophysique, Université de Liège, 4000 Liège, Belgium

¹⁹ Qatar Environment and Energy Research Institute (QEERI), HBKU, Qatar Foundation, PO Box 5825, Doha, Qatar

²⁰ Department of Astronomy, Boston University, 725 Commonwealth Avenue, Boston, MA 02215, USA

²¹ Istituto Nazionale di Fisica Nucleare, Sezione di Napoli, 80126 Napoli, Italy

²² Universität Hamburg, Meteorologisches Institut, Bundesstraße 55, 20146 Hamburg, Germany

²³ Astronomisches Rechen-Institut, Zentrum für Astronomie, Universität Heidelberg, Mönchhofstraße 12-14, 69120 Heidelberg, Germany

²⁴ Hamburger Sternwarte, Universität Hamburg, Gojenbergsweg 112, 21029 Hamburg, Germany

²⁵ Dipartimento di Fisica e Astronomia, Università di Bologna, Viale Berti Pichat 6/2, I-40127 Bologna, Italy

²⁶ Main Astronomical Observatory, Academy of Sciences of Ukraine, vul. Akademika Zabolotnoho 27, 03680 Kyiv, Ukraine

²⁷ European Southern Observatory, Karl-Schwarzschild-Straße 2, 85748 Garching bei München, Germany

²⁸ Space Telescope Science Institute, 3700 San Martin Drive, Baltimore, MD 21218, USA

²⁹ Jodrell Bank Centre for Astrophysics, University of Manchester, Oxford Road, Manchester M13 9PL, UK

³⁰ Finnish Centre for Astronomy with ESO (FINCA), University of Turku, Väisäläntie 20, FI-21500 Piikkiö, Finland

³¹ Department of Astronomy, Ohio State University, 140 W. 18th Ave., Columbus, OH 43210, USA

³² Department of Physics, Sharif University of Technology, P. O. Box 11155-9161 Tehran, Iran

³³ Planetary and Space Sciences, Department of Physical Sciences, The Open University, Milton Keynes, MK7 6AA, UK

20 August 2018

arXiv:1512.05549v2 [astro-ph.EP] 14 Mar 2016

ABSTRACT

We present 13 high-precision and four additional light curves of four bright southern-hemisphere transiting planetary systems: WASP-22, WASP-41, WASP-42 and WASP-55. In the cases of WASP-42 and WASP-55, these are the first follow-up observations since their discovery papers. We present refined measurements of the physical properties and orbital ephemerides of all four systems. No indications of transit timing variations were seen. All four planets have radii inflated above those expected from theoretical models of gas-giant planets; WASP-55 b is the most discrepant with a mass of $0.63 M_{\text{Jup}}$ and a radius of $1.34 R_{\text{Jup}}$. WASP-41 shows brightness anomalies during transit due to the planet occulting spots on the stellar surface. Two anomalies observed 3.1 d apart are very likely due to the same spot. We measure its change in position and determine a rotation period for the host star of 18.6 ± 1.5 d, in good agreement with a published measurement from spot-induced brightness modulation, and a sky-projected orbital obliquity of $\lambda = 6 \pm 11^\circ$. We conclude with a compilation of obliquity measurements from spot-tracking analyses and a discussion of this technique in the study of the orbital configurations of hot Jupiters.

Key words: stars: planetary systems — stars: fundamental parameters — stars: individual: WASP-22, WASP-41, WASP-42, WASP-55

1 INTRODUCTION

Of the over 1200 transiting extrasolar planets (TEPs) now known¹, the short-period gas-giant planets are of particular interest. These ‘hot Jupiters’ are the easiest to find due to their deep transits and high orbital frequency, are the most amenable to detailed characterisation due to their large masses and radii, and have highly irradiated and often rarefied atmospheres in which many physical phenomena are observable.

Most of the transiting hot Jupiters have been discovered by ground-based surveys studying bright stars. The brightness of the host stars is also extremely helpful in further characterisation of these objects via transmission spectroscopy and orbital obliquity studies. We are therefore undertaking a project to study TEPs orbiting bright host stars visible from the Southern hemisphere. Here we present transit light curves of four targets discovered by the WASP project (Pollacco et al. 2006) and measure their physical properties and orbital ephemerides to high precision.

WASP-22 was discovered by Maxted et al. (2010), who found it to be a low-density planet (mass $0.56 M_{\text{Jup}}$, radius $1.12 R_{\text{Jup}}$) orbiting a $V = 11.7$ solar-type star every 3.53 d. A linear trend in the radial velocities (RVs) was noticed and attributed to the presence of a third body in the system, which could be an M-dwarf, white dwarf or second planet. The trend in the RVs has been confirmed by Knutson et al. (2014), who measured the change in the systemic velocity of the system to be $\dot{\gamma} = 21.3^{+2.8}_{-2.7} \text{ m s}^{-1} \text{ yr}^{-1}$. Anderson et al. (2011) measured the projected orbital obliquity of the system to be $\lambda = 22^\circ \pm 16^\circ$ via the Rossiter-McLaughlin effect.

WASP-41 was announced by Maxted et al. (2011b) to be a hot Jupiter of mass $0.94 M_{\text{Jup}}$, radius $1.06 R_{\text{Jup}}$, and orbital period $P_{\text{orb}} = 3.05$ d. Its host is a $V = 11.6$ G8 V star showing magnetic activity indicative of a young age, and rotational modulation on a period of 18.41 ± 0.05 d. Neveu-VanMalle et al. (2015) obtained further spectroscopic RV measurements from which they

measured $\lambda = 29^{+10}_{-14}$ and detected a third object in the system with $P_{\text{orb}} = 421 \pm 2$ d and a minimum mass of $3.18 \pm 0.20 M_{\text{Jup}}$.

WASP-42 was discovered by Lendl et al. (2012) and is a low-density planet (mass $0.50 M_{\text{Jup}}$, radius $1.12 R_{\text{Jup}}$) orbiting a $V = 12.6$ star of spectral type K1 V every 4.98 d. An orbital eccentricity of $e = 0.060 \pm 0.0013$ was found by these authors, which is small but significant (Lucy & Sweeney 1971). No other study of the WASP-42 system has been published.

WASP-55 was one of a batch of new TEPs announced by Hellier et al. (2012) and is the lowest-density of the four planets considered here, with a mass of $0.50 M_{\text{Jup}}$ and radius of $1.30 R_{\text{Jup}}$. Its host is a G1 V star with a slightly sub-solar metallicity, and the P_{orb} of the system is 4.47 d. No other study of the WASP-55 system has been published, but it was a target in Field 6 of the K2 mission (Howell et al. 2014) and these observations will soon be available.

2 OBSERVATIONS AND DATA REDUCTION

We observed a total of 13 transits with the DFOSC (Danish Faint Object Spectrograph and Camera) instrument installed on the 1.54 m Danish Telescope at ESO La Silla, Chile. DFOSC has a field of view of $13.7' \times 13.7'$ at a plate scale of $0.39'' \text{ pixel}^{-1}$. We defocussed the telescope in order to improve the precision and efficiency of our observations (Southworth et al. 2009). The CCD was windowed during some observing sequences in order to shorten the readout time, and no binning was used. In most cases the night was photometric; observations taken through thin cloud were carefully checked and rejected if their reliability was questionable. The data were taken through either a Bessell R or Bessell I filter. An observing log is given in Table 1 and the final light curves are plotted in Fig. 1. All observations were taken after the upgrade of the telescope and CCD controller in 2011 (Southworth et al. 2014).

We reduced the data using the DEFOT pipeline (see Southworth et al. 2014, and references therein), which in turn uses the IDL² implementation of the APER routine from DAOPHOT (Stetson 1987) contained in the NASA ASTROLIB library³. For

* Based on data collected by MiNDSTeP with the Danish 1.54 m telescope at the ESO La Silla Observatory.

† Royal Society University Research Fellow

¹ See Transiting Extrasolar Planet Catalogue (TEPCat; Southworth 2011): <http://www.astro.keele.ac.uk/jkt/tepcat/>

² <http://www.exelisvis.co.uk/ProductsServices/IDL.aspx>

³ <http://idlastro.gsfc.nasa.gov/>

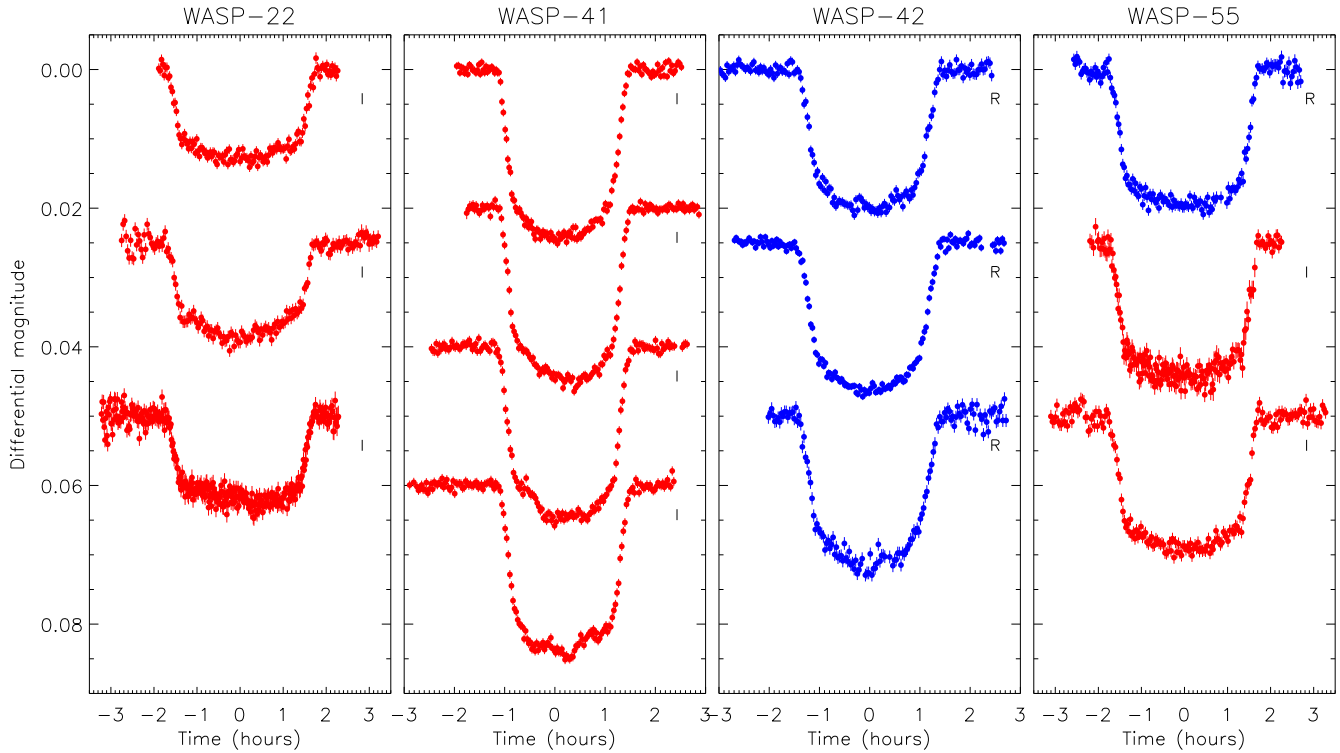


Figure 1. DFOSC light curves presented in this work, in the order they are given in Table 1. Times are given relative to the midpoint of each transit, and the filter used is indicated. Blue and red filled circles represent observations through the Bessell *R* and *I* filters, respectively.

Table 1. Log of the observations presented in this work. N_{obs} is the number of observations, T_{exp} is the exposure time, T_{dead} is the dead time between exposures, ‘Moon illum.’ is the fractional illumination of the Moon at the midpoint of the transit, given in italics if the Moon was down at that time, and N_{poly} is the order of the polynomial fitted to the out-of-transit data. The aperture radii refer to the target aperture, inner sky and outer sky, respectively.

Target	Telescope	Date of first obs	Start time (UT)	End time (UT)	N_{obs}	T_{exp} (s)	T_{dead} (s)	Filter	Airmass	Moon illum.	Aperture radii (px)	N_{poly}	Scatter (mmag)
WASP-22	84 cm	2011 12 01	00:21	05:56	353	45	12	none	1.38 → 1.00 → 1.19	0.365	17 65 100	2	1.680
WASP-22	84 cm	2012 01 23	00:54	04:53	228	45	10	none	1.02 → 1.02 → 2.46	<i>0.002</i>	15 38 60	2	1.646
WASP-22	Danish	2012 09 19	05:34	09:43	133	100	13	<i>I</i>	1.25 → 1.00 → 1.06	<i>0.137</i>	18 32 50	1	0.703
WASP-22	Danish	2013 09 25	03:10	09:08	172	100	25	<i>I</i>	2.21 → 1.00 → 1.05	0.680	18 25 55	1	0.913
WASP-22	Danish	2015 09 05	04:38	10:08	369	35–45	12	<i>I</i>	2.11 → 1.00 → 1.03	0.510	14 20 40	1	1.087
WASP-41	84 cm	2011 02 07	06:39	09:44	182	50	16	<i>R</i>	1.07 → 1.00 → 1.07	<i>0.161</i>	25 50 100	2	2.942
WASP-41	84 cm	2012 01 21	06:15	09:40	102	90	7	none	1.33 → 1.01 → 1.01	<i>0.045</i>	27 54 108	2	1.729
WASP-41	Danish	2014 05 31	00:35	05:03	155	80–100	13	<i>I</i>	1.01 → 1.00 → 1.71	<i>0.055</i>	22 30 55	1	0.571
WASP-41	Danish	2015 05 10	22:51	03:28	148	100	13	<i>I</i>	1.37 → 1.00 → 1.05	<i>0.548</i>	22 28 50	2	0.596
WASP-41	Danish	2015 05 13	23:25	04:30	159	100	13	<i>I</i>	1.19 → 1.00 → 1.19	<i>0.214</i>	17 27 45	2	0.646
WASP-41	Danish	2015 05 17	00:14	05:30	166	100	13	<i>I</i>	1.06 → 1.00 → 1.50	<i>0.015</i>	22 28 50	1	0.646
WASP-42	Danish	2013 05 25	00:51	06:28	164	100	20	<i>R</i>	1.04 → 1.03 → 2.10	1.000	20 28 45	2	0.673
WASP-42	Danish	2013 06 18	23:11	04:33	168	100	16	<i>R</i>	1.04 → 1.03 → 1.92	0.745	19 27 50	1	0.501
WASP-42	Danish	2013 06 28	23:00	03:43	143	100	15	<i>R</i>	1.04 → 1.03 → 1.82	<i>0.623</i>	22 30 55	1	0.924
WASP-55	Danish	2013 05 04	02:26	07:42	152	90–98	25	<i>R</i>	1.05 → 1.02 → 1.94	<i>0.314</i>	17 42 80	1	0.815
WASP-55	Danish	2014 06 18	22:56	03:26	206	50–110	11	<i>I</i>	1.10 → 1.02 → 1.35	<i>0.583</i>	13 42 80	1	1.144
WASP-55	Danish	2015 04 23	01:06	07:29	184	100	25	<i>I</i>	1.41 → 1.02 → 1.45	<i>0.231</i>	16 26 50	1	0.899

each dataset, the apertures were placed by hand on a reference image. Shifts between the individual images and the reference image were measured by cross-correlation, and applied to the aperture positions. The radii of the object aperture and sky annulus were chosen to minimise the scatter in the final light curve (see Table 1). The science images were not calibrated using bias or flat-field frames

as these tend to have little effect on the final light curves beyond a slight increase in the scatter of the datapoints.

We observed two transits of WASP-22 and two transits of WASP-41 using the 84 cm telescope at Observatorio Cerro Armazones in Antofagasta, Chile (currently decommissioned). Three transits were observed using an SBIG ST-10 CCD camera, giving a field of view of $15.6' \times 10.5'$ at a plate scale of $0.43'' \text{ pixel}^{-1}$, and

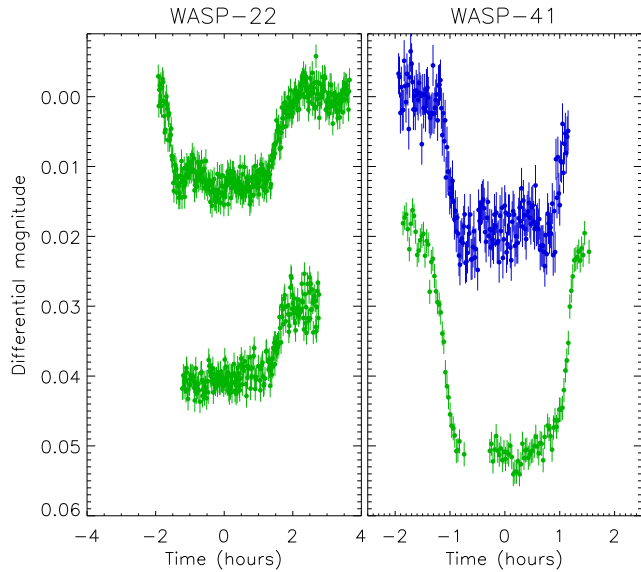


Figure 2. 84 cm telescope light curves presented in this work, in the order they are given in Table 1. Times are given relative to the midpoint of each transit, and the filter used is indicated. Blue and green filled circles represent observations through the R filter and without filter, respectively.

the first transit of WASP-41 was monitored using an SBIG STL CCD camera with a field of view of $29.3' \times 19.5'$ at a plate scale of $0.57'' \text{ pixel}^{-1}$. We defocussed the telescope and windowed the CCDs, and observed unfiltered except for the first transit of WASP-41 which was seen through an R filter. Data reduction was performed using a custom pipeline based on Starlink routines, including calibration with dark frames but not flat-fields. The PHOTOM package (Eaton et al. 1999) was used to perform aperture photometry, and the apertures were placed by hand. A growth-curve analysis was performed for each dataset in order to find the aperture size which gave the lowest scatter. The data are plotted in Fig. 2

For all datasets, differential-magnitude light curves were generated for each target star versus an ensemble comparison star containing the weighted flux sum of the best three to five comparison stars. A polynomial was also fitted to the observations outside transit and subtracted to rectify the final light curve to zero differential magnitude. In most cases a first-order polynomial was an adequate match to the slow brightness variations seen throughout the observing sequences, but in some cases a quadratic was required (see Table 1). The coefficients of the polynomial and the weights of the comparison stars were simultaneously optimised to minimise the scatter in the datapoints outside eclipse.

Manual time checks were obtained for several frames and the FITS file timestamps were confirmed to be on the UTC system to within a few seconds. They were then converted to the BJD(TDB) timescale (Eastman et al. 2010). The light curves are shown in Fig. 1, and the reduced data (Table 2) will be made available at the CDS⁴.

Finally, each of the light curves was fitted with the JKTEBOP code (see below) in order to determine the quality of fit and the times of midpoint of the transits. The errorbars for each dataset were rescaled to give a reduced χ^2 of $\chi^2_{\nu} = 1.0$ versus the fitted model, necessary as the uncertainties from the APER algorithm are often underestimated.

⁴ <http://vizier.u-strasbg.fr/>

Table 2. The first line of each of the light curves presented in this work. The full dataset will be made available at the CDS.

Target	Telescope	Filter	BJD(TDB) −2400000	Diff. mag.	Uncertainty
WASP-22	84 cm	none	55896.520223	−0.00291	0.00168
WASP-22	84 cm	none	55949.539861	−0.01180	0.00165
WASP-22	Danish	I	56189.736334	−0.00015	0.00074
WASP-22	Danish	I	56560.637168	−0.00034	0.00096
WASP-22	Danish	I	57270.696685	−0.00032	0.00105
WASP-41	84 cm	R	55599.780710	−0.00329	0.00294
WASP-41	84 cm	none	55947.763186	−0.00187	0.00173
WASP-41	Danish	I	56808.529719	−0.00050	0.00054
WASP-41	Danish	I	57153.458491	0.00071	0.00089
WASP-41	Danish	I	57156.481701	0.00025	0.00068
WASP-41	Danish	I	57159.515981	−0.00007	0.00065
WASP-42	Danish	R	56437.541226	0.00099	0.00061
WASP-42	Danish	R	56462.470118	−0.00036	0.00049
WASP-42	Danish	R	56472.461607	0.00013	0.00097
WASP-55	Danish	R	56416.608745	−0.00146	0.00083
WASP-55	Danish	I	56827.462644	−0.00027	0.00105
WASP-55	Danish	I	57135.553466	0.00004	0.00094

3 LIGHT CURVE ANALYSIS

We modelled the light curves of the four targets using the *Homogeneous Studies* methodology (see Southworth 2012 and references therein), which utilises the JKTEBOP⁵ code (Southworth 2013, and references therein). JKTEBOP represents the star and planet as spheres for the calculation of eclipse shapes and as bi-axial spheroids for proximity effects.

The fitted parameters in our analysis were the fractional radii of the star and planet (r_A and r_b), the orbital inclination (i), limb darkening coefficients, and a reference time of mid-transit. The fractional radii are the ratio between the true radii and the semi-major axis: $r_{A,b} = \frac{R_{A,b}}{a}$, and were expressed as their sum and ratio, $r_A + r_b$ and $k = \frac{r_b}{r_A}$, as these quantities are less strongly correlated. The orbital periods were fixed at the values found in Section 6. A polynomial of brightness versus time was applied to each transit light curve, with a polynomial order as given in Table 1. This is not needed to fit the data, as the polynomial has already been removed at the data reduction stage, but is necessary to include the uncertainties of polynomial fit in the errorbars of the photometric parameters (see Southworth et al. 2014).

Limb darkening (LD) was incorporated into the photometric model using each of five LD laws (see Southworth 2008), with the linear coefficients either fixed at theoretically predicted values⁶ or included as fitted parameters. We did not calculate fits for both LD coefficients in the four two-parameter laws as they are strongly correlated (Southworth 2008; Carter et al. 2008). The nonlinear coefficients were instead perturbed by ± 0.1 on a flat distribution during the error analysis simulations, in order to account for uncertainties in the theoretical coefficients.

All four targets have been observed in the HITEP high-resolution imaging campaign by Evans et al. (2015) using the Two Colour Imager (TCI) (Skottfelt et al. 2015) to perform Lucky Imag-

⁵ JKTEBOP is written in FORTRAN77 and the source code is available at <http://www.astro.keele.ac.uk/jkt/codes/jktebop.html>

⁶ Theoretical LD coefficients were obtained by bilinear interpolation to the host star's T_{eff} and $\log g$ using the JKTLD code available from: <http://www.astro.keele.ac.uk/jkt/codes/jktld.html>

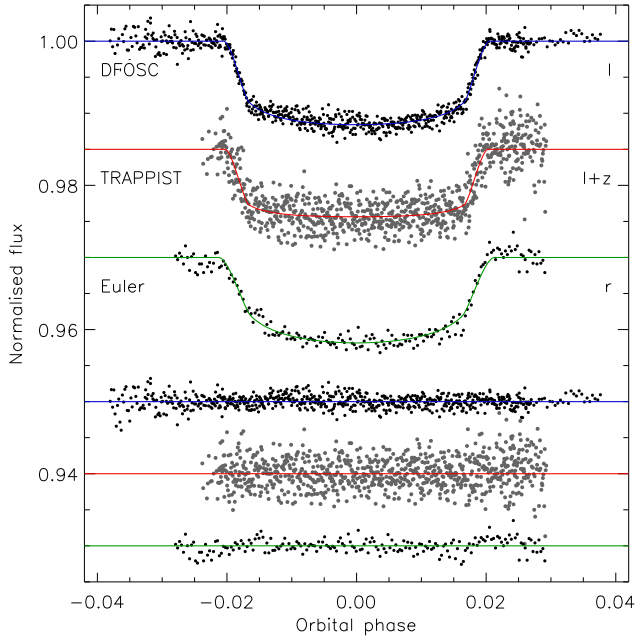


Figure 3. The phased light curves of WASP-22 analysed in this work, compared to the JKTEBOP best fits. The residuals of the fits are plotted at the base of the figure, offset from unity. Labels give the source and passband for each dataset. The polynomial baseline functions have been subtracted from the data before plotting.

ing. No stars were found close enough to WASP-22, WASP-41 or WASP-42 to affect our photometry. However, one star was found at an angular distance of 4.345 ± 0.010 arcsec from WASP-55, and was accounted for in the JKTEBOP model (see below).

Error estimates for the fitted parameters were obtained in several ways. We ran solutions using different LD laws, and also calculated errorbars using residual-permutation and Monte Carlo algorithms (Southworth 2008). The final value for each parameter is the unweighted mean of the four values from the solutions using the two-parameter LD laws. Its errorbar was taken to be the larger of the Monte-Carlo or residual-permutation alternatives, with an extra contribution to account for variations between solutions with the different LD laws. Tables of results for each light curve can be found in the Supplementary Information.

3.1 WASP-22

The three DFOSC light curves of WASP-22 were fitted simultaneously (Table 3 and Fig. 3). A circular orbit was assumed as Anderson et al. (2011) found $e < 0.063$ at the 3σ level, and Pont et al. (2011) found $e < 0.059$ at the 95% confidence level. The overall quality of the fit is $\chi^2_\nu = 1.01$ (remember that the errorbars on each dataset were already scaled to give $\chi^2_\nu = 1.0$) which shows that the three light curves give highly consistent transit shapes.

Anderson et al. (2011) included in their analysis three new transit light curves of WASP-22, two from the TRAPPIST telescope (Jehin et al. 2011) and one from EulerCam on the Euler telescope (Lendl et al. 2012). We modelled these in the same way as used for our own data. The follow-up light curve presented by Maxted et al. (2010) has only partial coverage of one transit so we did not consider it further in the current work. The full results for WASP-22 are given in Table 3 and show an acceptable agree-

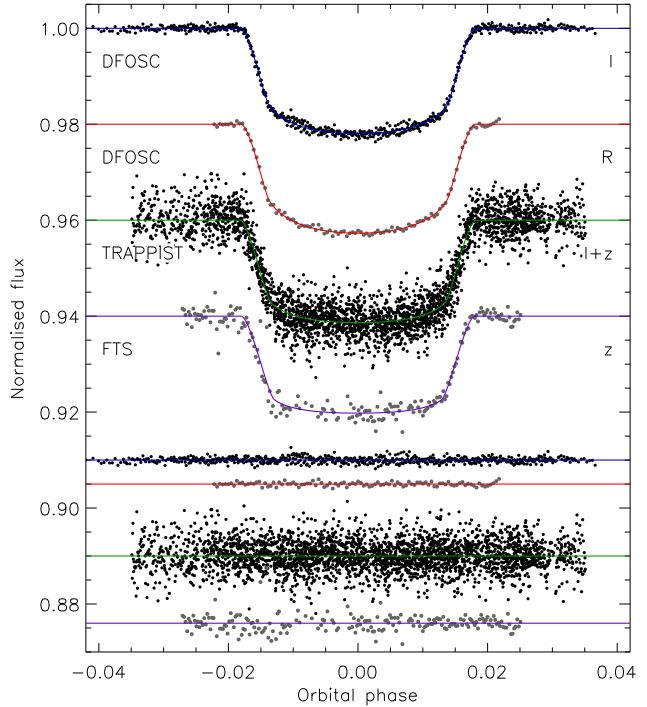


Figure 4. As Fig. 3, but for WASP-41.

ment between the different datasets. For our final values we adopt the weighted means of the individual measurements, calculated by multiplying the probability density functions of the measurements. The final values are consistent with, and an improvement on, previously published values.

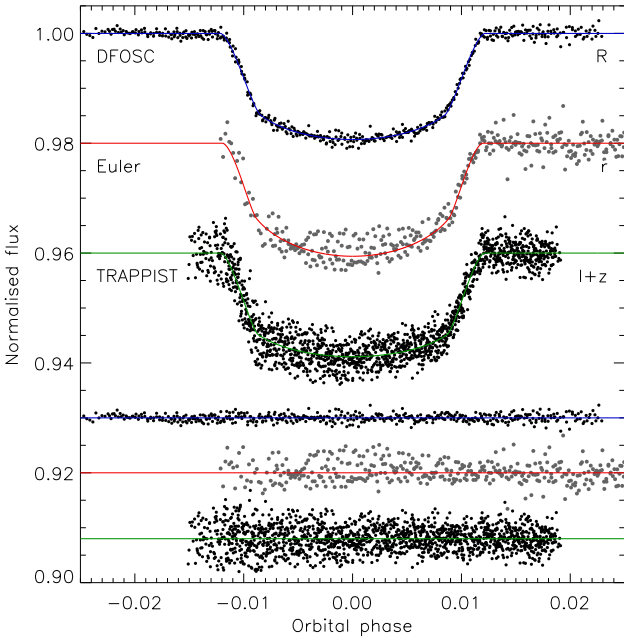
3.2 WASP-41

WASP-41 is a trickier system because there are anomalies due to starspot-crossing events in at least two of our high-precision light curves. In the current part of the analysis these were ignored, in order to maintain homogeneity of approach, so were therefore basically treated as red noise. A detailed analysis of the spot anomalies will be presented below. Our four DFOSC light curves of WASP-41 were fitted simultaneously (Table 3 and Fig. 4), for which the best fit returns $\chi^2_\nu = 1.05$ despite the presence of the spot anomalies. A circular orbit was assumed as Neveu-VanMalle et al. (2015) found $e < 0.026$ at the 2σ confidence level.

As with WASP-22, the discovery paper of WASP-41 included only one high-precision light curve, which does not cover the full transit. This dataset was not analysed here due to the weak constraints on system properties from light curves missing coverage of the third and fourth contact points in the eclipse. However, Neveu-VanMalle et al. (2015) presented eight new light curves of WASP-41 obtained from three telescopes. The single complete transit from the Danish Telescope, labelled ‘DFOSC R’ in Fig. 4, and the transit from Faulkes Telescope South (FTS) were each modelled in isolation. The five datasets from TRAPPIST were modelled together, with an extra polynomial to account for the meridian flip at JD 2456402.653 (L. Delrez, 2015, priv. comm.). The final results are shown in Table 3 and agree with, but improve on, published values.

Table 3. Parameters of the JKTEBOP fits to the new and published light curves of the four planetary systems.

System	Source	Filter	$r_A + r_b$	k	i ($^\circ$)	r_A	r_b
WASP-22	DFOSC	I	$0.1284^{+0.0039}_{-0.0017}$	$0.0996^{+0.0013}_{-0.0012}$	$89.3^{+1.0}_{-1.3}$	$0.1168^{+0.0035}_{-0.0015}$	$0.01163^{+0.00048}_{-0.00020}$
WASP-22	TRAPPIST	$I+z$	$0.1327^{+0.0083}_{-0.0059}$	$0.0951^{+0.0015}_{-0.0013}$	$87.9^{+2.1}_{-2.3}$	$0.1212^{+0.0074}_{-0.0053}$	$0.01152^{+0.00084}_{-0.00058}$
WASP-22	Euler	r	$0.1404^{+0.0121}_{-0.0090}$	$0.0982^{+0.0041}_{-0.0049}$	$87.1^{+2.6}_{-1.7}$	$0.1278^{+0.0103}_{-0.0078}$	$0.01255^{+0.00168}_{-0.00112}$
<i>Weighted mean</i>			$0.1310^{+0.0031}_{-0.0028}$	$0.0978^{+0.0012}_{-0.0012}$	$88.6^{+1.0}_{-1.0}$	$0.1193^{+0.0027}_{-0.0026}$	$0.01172^{+0.00039}_{-0.00025}$
WASP-41	DFOSC	I	0.1143 ± 0.0013	0.1362 ± 0.0008	89.07 ± 0.53	0.1006 ± 0.0011	0.01369 ± 0.00021
WASP-41	DFOSC	R	0.1128 ± 0.0015	0.1369 ± 0.0013	89.62 ± 1.06	0.0992 ± 0.0013	0.01358 ± 0.00027
WASP-41	TRAPPIST	$I+z$	0.1176 ± 0.0034	0.1378 ± 0.0019	88.26 ± 0.98	0.1034 ± 0.0028	0.01424 ± 0.00053
WASP-41	FTS	z	0.1198 ± 0.0054	0.1366 ± 0.0018	87.63 ± 0.80	0.1054 ± 0.0047	0.01440 ± 0.00078
<i>Weighted mean</i>			0.1142 ± 0.0009	0.1365 ± 0.0006	88.70 ± 0.39	0.1004 ± 0.0008	0.01373 ± 0.00015
WASP-42	DFOSC	R	0.0851 ± 0.0027	0.1296 ± 0.0009	87.91 ± 0.19	0.0753 ± 0.0024	0.00976 ± 0.00034
WASP-42	Euler	r	0.0794 ± 0.0047	0.1275 ± 0.0047	88.72 ± 1.01	0.0704 ± 0.0040	0.00897 ± 0.00071
WASP-42	TRAPPIST	$I+z$	0.0829 ± 0.0033	0.1284 ± 0.0016	88.23 ± 0.36	0.0735 ± 0.0028	0.00943 ± 0.00043
<i>Weighted mean</i>			0.0834 ± 0.0019	0.1293 ± 0.0008	88.00 ± 0.17	0.0739 ± 0.0017	0.00955 ± 0.00025
WASP-55	DFOSC	R	$0.1025^{+0.0030}_{-0.0009}$	$0.1253^{+0.0014}_{-0.0010}$	$89.83^{+0.57}_{-1.20}$	$0.0911^{+0.0026}_{-0.0008}$	$0.01141^{+0.00044}_{-0.00012}$
WASP-55	DFOSC	I	$0.1028^{+0.0024}_{-0.0008}$	$0.1236^{+0.0009}_{-0.0008}$	$89.73^{+0.59}_{-0.93}$	$0.0915^{+0.0021}_{-0.0007}$	$0.01130^{+0.00033}_{-0.00012}$
WASP-55	Euler	r	$0.1102^{+0.0064}_{-0.0064}$	$0.1274^{+0.0024}_{-0.0025}$	$87.79^{+0.98}_{-0.86}$	$0.0978^{+0.0055}_{-0.0054}$	$0.01246^{+0.00085}_{-0.00088}$
<i>Weighted mean</i>			$0.1033^{+0.0018}_{-0.0010}$	$0.1246^{+0.0007}_{-0.0007}$	$89.05^{+0.59}_{-0.59}$	$0.0918^{+0.0015}_{-0.0009}$	$0.01143^{+0.00025}_{-0.00013}$

**Figure 5.** As Fig. 3, but for WASP-42.

3.3 WASP-42

Of the four systems studied in this work, WASP-42 is the only one with an eccentric orbit. Lendl et al. (2012) found that their measurement of a small eccentricity was significant at the 99.5% level. We accounted for this in the JKTEBOP modelling by constraining the eccentricity and argument of periastron to be $e = 0.060 \pm 0.013$ and $\omega = 167 \pm 26^\circ$, respectively. There also appears to be a starspot crossing event just after the midpoint of the third and final transit, which is not surprising given the T_{eff} of the host star. We did not make any attempt to fit this anomaly because it has a low amplitude and no other spot anomalies were seen.

Our three light curves were all obtained within 34 d – the observability of transits in this object has a strong seasonal dependence because its orbital period is close to an integer number of days – and were modelled together (Table 3). The combined fit has $\chi^2_\nu = 1.09$, once again showing good agreement between our three light curves (Fig. 5). We also modelled the light curves from the Euler and TRAPPIST telescopes presented in Lendl et al. (2012), which cover two and four transits respectively. The three light curves are in excellent agreement, with values of χ^2_ν between 0.30 and 0.57 for the photometric parameters, where χ^2_ν is calculated for the individual values of a parameter versus to the weighted mean of the values.

3.4 WASP-55

From high-resolution imaging Evans et al. (2015) found a faint star close to the WASP-55 system. The star is at an angular distance of 4.345 ± 0.010 arcsec and has a magnitude difference of 5.210 ± 0.018 in the r_{TCI} band, which is similar to a combined Gunn $i+z$ band. No observations were obtained in the v_{TCI} band, so the colour and therefore spectral type of the faint companion cannot be constrained. We conservatively find that between 50% and 90% of the total light from this object is contained in the aperture used for WASP-55 itself, giving a contaminating light fraction of 0.41% to 0.74%. We account for this in the JKTEBOP fits by setting the third light parameter to be $L_3 = 0.006 \pm 0.003$, where the errorbar has been increased to account for possible differences between the r_{TCI} band used for the high-resolution images and the R and I bands used in the current work.

We observed three transits of WASP-55, one with an R filter and two through an I filter. The two datasets were modelled separately but both with the third light constraint (Fig. 6). The results (Table 3) are in good agreement. The discovery paper (Hellier et al. 2012) presented TRAPPIST light curves of two transits and a Euler light curve of one transit. Both TRAPPIST datasets have only partial coverage of the transit so were not analysed here. The Euler light curve is of decent quality albeit showing significant red

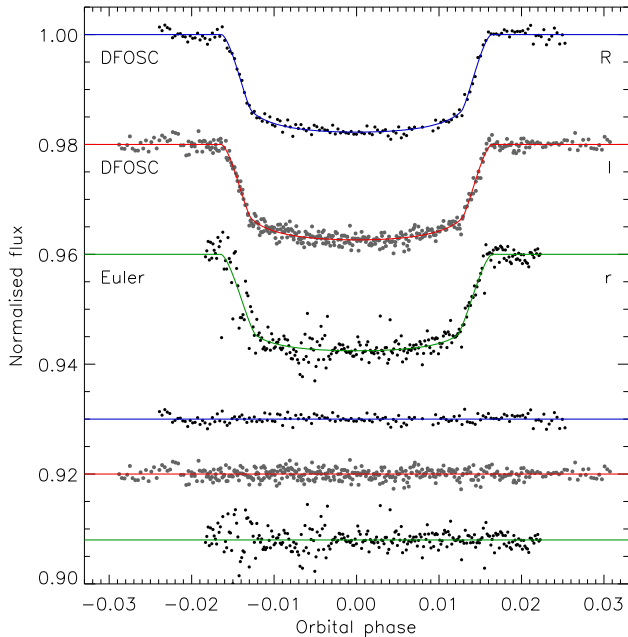


Figure 6. As Fig. 3, but for WASP-55.

Table 4. Spectroscopic properties of the planet host stars used in the determination of the physical properties of the systems.

References: (1) Mortier et al. (2013); (2) Knutson et al. (2014); (3) Neveu-VanMalle et al. (2015); (4) Lendl et al. (2012); (5) Hellier et al. (2012)

Target	T_{eff} (K)	$[\frac{\text{Fe}}{\text{H}}]$ (dex)	K_A (m s^{-1})	Refs.
WASP-22	6153 ± 50	0.26 ± 0.05	70.9 ± 1.6	1,1,2
WASP-41	5546 ± 50	0.06 ± 0.05	138 ± 2	1,1,3
WASP-42	5315 ± 79	0.29 ± 0.05	64.8 ± 1.7	1,1,4
WASP-55	6070 ± 53	0.09 ± 0.05	70 ± 4	1,1,5

noise, and was modelled with JKTEBOP in the same way as for our own data. As with WASP-22, we obtain weighted means of the photometric parameters by multiplying together the probability density functions of the individual measurements for each parameter. We find χ^2_{ν} values less than 1.0 for all photometric parameters, indicating that the results for the different light curves are in good agreement.

4 PHYSICAL PROPERTIES

The results of the above photometric analysis were combined with measured spectroscopic quantities in order to determine the physical properties of the four planetary systems. For each object we used the weighted mean of the measured values of r_A , r_b and i from Table 3. To these we added spectroscopic values for the host star’s effective temperature, T_{eff} , metallicity, $[\frac{\text{Fe}}{\text{H}}]$, and velocity amplitude, K_A , from the literature (see Table 4). These quantities alone are insufficient to yield the physical properties of the stars or planets, so the properties of the host stars were additionally constrained using tabulated predictions from theoretical models (Claret 2004; Demarque et al. 2004; Pietrinferni et al. 2004; VandenBerg et al. 2006; Dotter et al. 2008).

For each object we estimated the value of the velocity ampli-

tude of the planet, K_b and calculated the physical properties of the system using this and the measured quantities. We then iteratively adjusted K_b to obtain the best agreement between the calculated $\frac{R_A}{a}$ and the measured r_A , and between the T_{eff} and that predicted by the stellar models for the observed $[\frac{\text{Fe}}{\text{H}}]$ and calculated stellar mass (M_A). This was done for a range of ages, allowing us to identify the overall best fit and age of the system (see Southworth 2009). This process was performed for each of the five sets of theoretical models, allowing us to quantify the effect of using theoretical predictions on our results.

The measured physical properties of the four systems are given in Table 5. Statistical errors were calculated by propagating the uncertainties in all the input quantities to each of the output quantities. Systematic uncertainties were obtained by taking the maximum deviation between the final value and the five values from using the different stellar models. Our results are in good agreement with literature values for three of the four systems, but differ in that they are based on more extensive observational data and explicitly account for systematic errors due to the use of theoretical stellar models.

In the case of WASP-22, our measured system properties differ moderately from previous values (Maxted et al. 2010; Anderson et al. 2011). Whilst there are some differences in the photometric parameters from our data, which are of significantly higher quality than the existing TRAPPIST and Euler light curves, the main effect is due to our adoption of the higher and more precise T_{eff} value obtained by Mortier et al. (2013) for the host star. For comparison, we calculated an alternative set of results using the lower value of $T_{\text{eff}} = 6020 \pm 50$ K found from the infrared flux method by Maxted et al. (2011a). The mass and radius of the host star change to $1.194 M_{\odot}$ and $1.236 R_{\odot}$, respectively, and those of the planet to $0.598 M_{\text{Jup}}$ and $1.181 R_{\text{Jup}}$. These numbers are all smaller than our adopted values, but in all cases the change is within the errorbars.

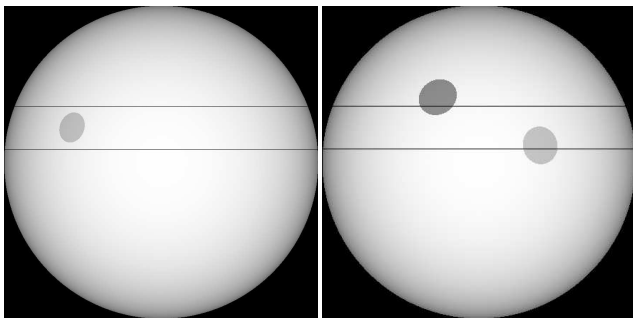
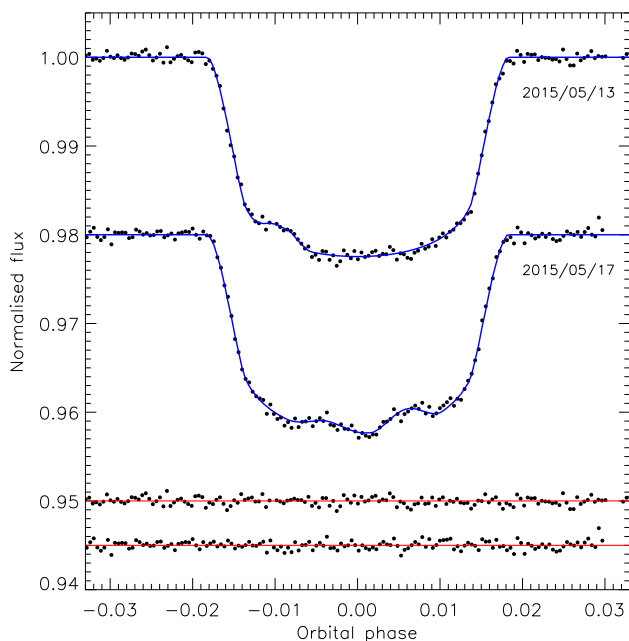
5 SPOT MODELLING OF WASP-41

The third and fourth transits of WASP-41 show clear evidence of starspot activity, manifested as short increases in brightness during transit when the planet crosses areas which are of lower surface brightness than the rest of the stellar photosphere (see Fig. 1). The spot crossing events hold information on the size and brightness of the spots, and potentially allow the motion of spots and therefore the rotation of the star to be tracked (Silva-Valio 2008; Nutzman et al. 2011). It was for this reason that we observed three transits of WASP-41 over a six-day period in 2015.

We modelled these two transit light curves using the PRISM and GEMC codes (Tregloan-Reed et al. 2013, 2015). PRISM uses a pixellation approach to calculate the light curve of a planet transiting a spotted star, and GEMC is a hybrid between a Markov chain Monte Carlo and a genetic algorithm to find the best fit to a light curve of a single transit. GEMC is based on the differential evolution Markov chain approach by Ter Braak (2006). The light curve from the night of 2015/05/13 shows clear evidence for one spot crossing – attempts to fit for a postulated second spot crossing did not lead to a determinate solution – and the light curve from the night of 2015/05/17 contains two spot crossing events. These two datasets were fitted individually in order to determine the locations, sizes and contrasts of the spots, where ‘contrast’ refers to the ratio of the brightness of the spot to that of the pristine stellar photosphere in the passband used to obtain the observations (Figs. 7 and 8).

Table 5. Derived physical properties of the four systems. Where two sets of errorbars are given, the first is the statistical uncertainty and the second is the systematic uncertainty.

Quantity	Symbol	WASP-22	WASP-41	WASP-42	WASP-55
Stellar mass (M_{\odot})	M_A	$1.249^{+0.073}_{-0.030}^{+0.015}_{-0.014}$	$0.987 \pm 0.021 \pm 0.026$	$0.951 \pm 0.037 \pm 0.051$	$1.162^{+0.029}_{-0.033}^{+0.022}_{-0.021}$
Stellar radius (R_{\odot})	R_A	$1.255^{+0.030}_{-0.029}^{+0.005}_{-0.005}$	$0.886 \pm 0.009 \pm 0.008$	$0.892 \pm 0.021 \pm 0.016$	$1.102^{+0.020}_{-0.015}^{+0.007}_{-0.007}$
Stellar surface gravity (c.g.s)	$\log g_A$	$4.338^{+0.027}_{-0.020}^{+0.002}_{-0.002}$	$4.538 \pm 0.008 \pm 0.004$	$4.515 \pm 0.022 \pm 0.008$	$4.419^{+0.009}_{-0.015}^{+0.003}_{-0.003}$
Stellar density (ρ_{\odot})	ρ_A	$0.632^{+0.043}_{-0.041}$	1.420 ± 0.034	1.338 ± 0.092	$0.869^{+0.026}_{-0.041}$
Planet mass (M_{Jup})	M_b	$0.617^{+0.028}_{-0.017}^{+0.005}_{-0.005}$	$0.977 \pm 0.020 \pm 0.017$	$0.527 \pm 0.020 \pm 0.019$	$0.627^{+0.037}_{-0.038}^{+0.008}_{-0.007}$
Planet radius (R_{Jup})	R_b	$1.199^{+0.046}_{-0.027}^{+0.005}_{-0.005}$	$1.178 \pm 0.015 \pm 0.010$	$1.122 \pm 0.033 \pm 0.020$	$1.335^{+0.031}_{-0.020}^{+0.008}_{-0.008}$
Planet surface gravity (m s^{-2})	g_b	$10.63^{+0.53}_{-0.71}$	17.45 ± 0.46	10.38 ± 0.61	$8.73^{+0.54}_{-0.62}$
Planet density (ρ_{Jup})	ρ_b	$0.334^{+0.024}_{-0.033}^{+0.001}_{-0.001}$	$0.558 \pm 0.020 \pm 0.005$	$0.349 \pm 0.029 \pm 0.006$	$0.247^{+0.017}_{-0.021}^{+0.001}_{-0.002}$
Equilibrium temperature (K)	T'_{eq}	1502^{+20}_{-20}	1242 ± 12	1021 ± 19	1300^{+15}_{-13}
Orbital semimajor axis (au)	a	$0.0489^{+0.0010}_{-0.0004}^{+0.0002}_{-0.0002}$	$0.0410 \pm 0.0003 \pm 0.0004$	$0.0561 \pm 0.0007 \pm 0.0010$	$0.0558^{+0.0005}_{-0.0005}^{+0.0004}_{-0.0003}$
Age (Gyr)	τ	$1.3^{+0.6}_{-1.7}^{+0.4}_{-0.2}$	$1.2^{+1.1}_{-0.0}^{+0.3}_{-0.2}$	$4.4^{+3.0}_{-2.4}^{+3.2}_{-2.4}$	$1.1^{+0.8}_{-0.6}^{+0.4}_{-0.1}$

**Figure 7.** Visualisations of the surface of WASP-41 A at the times of the third (left) and fourth (right) transits we observed with DFOSC, produced by PRISM. The boundaries of the path of the planet are shown with black lines and the spots are shown with their measured locations, sizes and contrasts.**Figure 8.** Best fits from PRISM+GEMC for the third (upper) and fourth (lower) transits we observed with DFOSC.**Table 6.** Properties of the spots occulted during two transits of WASP-41 A by WASP-41 b, obtained from modelling the light curves with PRISM+GEMC. Longitude and latitude are defined to be zero at the centre of the stellar disc.

Light curve	2015/05/13	2015/05/17	2015/05/17
Spot number	Spot 1		Spot 2
Spot longitude ($^{\circ}$)	-36.3 ± 4.5	-37.2 ± 2.8	23.7 ± 1.6
Spot latitude ($^{\circ}$)	15.3 ± 10.3	27.4 ± 6.6	8.3 ± 6.5
Spot size ($^{\circ}$)	10.4 ± 6.5	15.5 ± 3.5	14.3 ± 3.2
Spot contrast	0.80 ± 0.14	0.82 ± 0.07	0.89 ± 0.06

In order to limit the strong correlation between the orbital inclination (or, equivalently, the impact parameter) of the planet and the latitude of the spot, we fixed $i = 88.7^{\circ}$ in the PRISM+GEMC fits. We also fitted for the linear LD coefficient whilst fixing the quadratic coefficient to 0.3. Exploratory fits used a resolution of 15 pixels for the radius of the planet, for speed, and for final fits we used 50 pixels to obtain higher precision in the results (see Table 6).

We found that the latitudes of the spots are not very well determined, as expected for the case where the transit cord of the planet passes close to the centre of the star. Even in the case of a fixed spot contrast, a similar amplitude in flux for the spot crossing event can be obtained for a small spot which is totally occulted by the planet, or a larger spot positioned *either above or below the transit cord* which is partially eclipsed by the planet. Similarly, a partially-eclipsed spot can have very little effect on the light curve shape if a modest increase in its size is compensated for by moving its latitude further away from the transit cord, and vice versa. As there is also a known degeneracy between spot contrast and size (e.g. Tregloan-Reed et al. 2013), but only for those parts of the spot which are occulted by the planet, it is clear that the parameter space for spot-modelling is inherently complex and degenerate.

However, the spot longitudes are very well determined by our data (see Table 6) because they govern the times at which spot crossings are detected. We now assert that the spot observed on 2015/05/13 is the same as the second spot observed on 2015/05/17. In this case the change in the longitude and latitude of the spot (both defined to be zero at the centre of the stellar disc) are $60.0 \pm 4.8^{\circ}$ and $-7 \pm 12^{\circ}$, respectively, and the time difference between the midpoints of the two spot crossings is 3.097 ± 0.005 d. If the spot moved directly from the first to the second location, this gives a rotation period of 18.6 ± 1.5 d at a latitude of approxi-

mately 12° ⁷, in good agreement with the value of 18.41 ± 0.05 d measured from the spot-induced brightness modulation of WASP-41 A by Maxted et al. (2011b). This equates to a projected rotational velocity of $v \sin i = 2.4 \pm 0.2$ km s⁻¹, again in good agreement with the measurements from Maxted et al. (2011b) and Neveu-VanMalle et al. (2015). We also note that the measured radii and contrasts of the two spot events agree to within the (relatively large) errorbars.

The assumption that we have detected the same spot twice in two different positions on the stellar surface leads directly to a detection of a change of latitude and therefore a measurement of the sky-projected orbital obliquity of the system of $\lambda = 6 \pm 11^\circ$. Neveu-VanMalle et al. (2015) used spectroscopy during a transit of WASP-41 to measure $\lambda = 29^{+10}_{-14}^\circ$ with, and $\lambda = 48 \pm 29^\circ$ without, a Bayesian prior on the projected rotational velocity. Our revised value is consistent with both to within 1.3σ , removes the ambiguity due to choice of methodology, and also banishes the previous hints of orbital misalignment. WASP-41 is therefore another example of an aligned system containing a transiting hot Jupiter and a cool star with a precisely measured projected orbital obliquity.

6 TRANSIT TIMING ANALYSIS

Each of the transit light curves available for the four systems were fitted with the JKTEBOP code in order to determine the time of midpoint of the transit. We did not apply this analysis to light curves lacking complete coverage of a transit, as these give noisy and possibly biased values (e.g. Gibson et al. 2009). We also obtained the WASP-South light curves, divided them into individual observing seasons, and fit each season separately to obtain a time of minimum close to the midpoint of the data. In the case of the WASP-South data, which have a very high scatter compared to the follow-up light curves, we fixed the values of the photometric parameters to the best estimates obtained in Section 3 and thus fitted for only the time of midpoint and the out-of-transit brightness of the system. All measured transit times were moved to the TDB timescale.

We also included times of minimum for WASP-41 and WASP-55 from the Exoplanet Transit Database⁸ (Poddaný et al. 2010), which provides data and transit times from amateur observers affiliated with TRESCA⁹. We assumed that the times were on the UTC timescale and converted them to TDB.

For each object we fitted the times of mid-transit with straight lines to determine a new linear orbital ephemeris. Table 7 gives all transit times plus their residuals versus the fitted ephemeris. In cases where the χ_ν^2 was greater than 1.0 we scaled the uncertainties to give $\chi_\nu^2 = 1.0$. E gives the cycle count versus the reference epoch, and the bracketed numbers show the uncertainty in the final digit of the preceding number.

⁷ Alternative assumptions all yield much shorter rotation periods. For example, if the spot moves from the first to the second location but in a retrograde direction it has to travel 300° and the rotation period is 3.7 ± 0.3 d. If the rotation is instead prograde but the star rotates once plus the 60° difference in longitude, then the rotation period is 2.4 ± 0.2 d. All other possibilities require additional rotations of the star between the two detections of the spot, and thus yield ever-shorter rotation periods.

⁸ The Exoplanet Transit Database (ETD) can be found at: <http://var2.astro.cz/ETD/credit.php>

⁹ The TRansiting ExoplanetS and CANDidates (TRESCA) website can be found at: <http://var2.astro.cz/EN/tresca/index.php>

The new ephemeris for WASP-22 is based on eight timing measurements and is:

$$T_0 = \text{BJD(TDB)} 2\,455\,532.72776(22) + 3.53273064(70) \times E$$

where the fit has $\chi_\nu^2 = 1.46$. The timebase of the ephemeris was chosen to be close to the weighted mean of the data and coincides with the transit observed simultaneously by the TRAPPIST and Euler telescopes. The most discrepant timing is the measurement from TRAPPIST data at cycle -4 , which differs by 2.4σ from the timing predicted by the ephemeris. This is not sufficient grounds to reject the datapoint, so we did not do so. Instead, the errorbar for the ephemeris were multiplied by $\sqrt{1.46}$ to account for the excess χ_ν^2 .

For WASP-41 we have 19 timings and obtain the ephemeris:

$$T_0 = \text{BJD(TDB)} 2\,455\,996.67927(10) + 3.05240154(41) \times E$$

with $\chi_\nu^2 = 2.67$. This is the largest χ_ν^2 among the four objects in this work, and occurs for the system with the most active host star. The errorbars of the ephemeris have been inflated to account for the excess χ_ν^2 . The times of midpoint of the final two DFOC transits were obtained using PRISM+GEMC, which agree with the midpoints obtained using JKTEBOP to within 0.00015 d. This is in line with expectations for the effects of starspots (Barros et al. 2013; Oshagh et al. 2013; Ioannidis et al. 2016).

For WASP-42 there are three timings from data in the current work, five from published follow-up light curves and one from WASP-South observations in the 2008 season. Whilst there are plenty of WASP-South observations from 2006 and 2007, there is no coverage of transits due to the near-integer orbital period of the system. We find the ephemeris:

$$T_0 = \text{BJD(TDB)} 2\,455\,650.56728(15) + 4.9816819(11) \times E$$

where $\chi_\nu^2 = 1.35$ and the errorbars have been inflated to account for this.

For WASP-55 we have 11 timings which yield this ephemeris:

$$T_0 = \text{BJD(TDB)} 2\,456\,416.71565(13) + 4.4656291(11) \times E$$

with $\chi_\nu^2 = 1.10$ (accounted for in the errorbars).

Fig. 9 shows the residuals versus the linear ephemeris for each of our four targets. No transit timing variations are apparent, and there are too few timing measurements for a search for such variations to be useful. Our period values for all four systems are consistent with previous measurements but are significantly more precise due to the addition of new high-quality data and a longer temporal baseline.

7 SUMMARY AND CONCLUSIONS

WASP-22, WASP-41, WASP-42 and WASP-55 are four systems containing transiting hot Jupiters with large radii. We have presented high-precision photometry of 13 transits of the four systems, and used these data to refine their measured orbital ephemerides and physical properties. Our light curves of each system contain highly consistent transit shapes, demonstrating the repeatability of observations taken with the telescope-defocussing method. We find no evidence for transit timing variations in any of the systems, and our new measurements of the system properties are mostly in good agreement with previous determinations based on fewer and less precise data.

All four planets have inexplicably larger radii than expected from theoretical models (Bodenheimer et al. 2003; Fortney et al.

Table 7. Times of minimum light and their residuals versus the ephemerides derived in this work.

Target	Time of minimum (BJD/TDB)	Uncertainty (d)	Cycle number	Residual (d)	Reference
WASP-22	2454041.91397	0.00122	−422.0	−0.00146	This work (WASP-South 2006)
WASP-22	2454409.31798	0.00078	−318.0	−0.00143	This work (WASP-South 2007)
WASP-22	2455518.59851	0.00059	−4.0	0.00167	This work (TRAPPIST)
WASP-22	2455532.72730	0.00038	0.0	−0.00046	This work (Euler)
WASP-22	2455532.72761	0.00053	0.0	−0.00015	This work (TRAPPIST)
WASP-22	2455896.60029	0.00081	103.0	0.00128	This work (84 cm)
WASP-22	2456189.81595	0.00022	186.0	0.00029	This work (Danish)
WASP-22	2456560.75224	0.00029	291.0	−0.00014	This work (Danish)
WASP-22	2457270.83104	0.00022	492.0	−0.00020	This work (Danish)
WASP-41	2454201.86515	0.00180	−588.0	−0.00201	This work (WASP-South 2007)
WASP-41	2454549.83845	0.00100	−474.0	−0.00248	This work (WASP-South 2008)
WASP-41	2455642.60026	0.00027	−116.0	−0.00043	This work (TRAPPIST)
WASP-41	2455654.81018	0.00020	−112.0	−0.00012	This work (TRAPPIST)
WASP-41	2455663.96815	0.00024	−109.0	0.00065	This work (FTS)
WASP-41	2455694.49015	0.00091	−99.0	−0.00137	This work (TRAPPIST)
WASP-41	2455725.01389	0.00045	−89.0	−0.00164	Tan (ETD)
WASP-41	2455947.84052	0.00021	−16.0	−0.00032	This work (84 cm)
WASP-41	2455996.67838	0.00032	0.0	−0.00089	This work (TRAPPIST)
WASP-41	2456402.65000	0.00021	133.0	0.00132	This work (TRAPPIST)
WASP-41	2456402.64891	0.00007	133.0	0.00023	This work (Danish)
WASP-41	2456424.01544	0.00030	140.0	−0.00005	Tan (ETD)
WASP-41	2456698.73202	0.00038	230.0	0.00040	Masek (ETD)
WASP-41	2456765.88379	0.00093	252.0	−0.00067	Evans (ETD)
WASP-41	2456768.93761	0.00041	253.0	0.00075	Evans (ETD)
WASP-41	2456808.61760	0.00009	266.0	−0.00048	This work (Danish)
WASP-41	2456820.82714	0.00058	270.0	−0.00055	Evans (ETD)
WASP-41	2457153.53964	0.00009	379.0	0.00019	This work (Danish)
WASP-41	2457156.59146	0.00015	380.0	−0.00039	This work (Danish, PRISM+GEMC)
WASP-41	2457159.64436	0.00017	381.0	0.00011	This work (Danish, PRISM+GEMC)
WASP-42	2454554.59925	0.00140	−220.0	0.00199	This work (WASP-South 2008)
WASP-42	2455625.65818	0.00027	−5.0	−0.00070	This work (TRAPPIST)
WASP-42	2455630.64068	0.00029	−4.0	0.00012	This work (TRAPPIST)
WASP-42	2455650.56811	0.00033	0.0	0.00082	This work (TRAPPIST)
WASP-42	2455655.54875	0.00032	1.0	−0.00022	This work (TRAPPIST)
WASP-42	2455645.58567	0.00035	−1.0	0.00007	This work (Euler)
WASP-42	2456437.67306	0.00014	158.0	0.00004	This work (Danish)
WASP-42	2456462.58139	0.00010	163.0	−0.00004	This work (Danish)
WASP-42	2456472.54492	0.00018	165.0	0.00012	This work (Danish)
WASP-55	2453902.56555	0.00340	−563.0	−0.00093	This work (WASP-South 2006)
WASP-55	2454201.76435	0.00280	−496.0	0.00073	This work (WASP-South 2007)
WASP-55	2454581.34095	0.00220	−411.0	−0.00115	This work (WASP-South 2008)
WASP-55	2454951.98517	0.00210	−328.0	−0.00415	This work (WASP-South 2009)
WASP-55	2455309.24157	0.00170	−248.0	0.00192	This work (WASP-South 2010)
WASP-55	2455715.61277	0.00046	−157.0	0.00088	This work (Euler)
WASP-55	2456416.71548	0.00016	0.0	−0.00017	This work (Danish)
WASP-55	2456778.43544	0.00283	81.0	0.00383	Lomoz (ETD)
WASP-55	2456778.42973	0.00200	81.0	−0.00188	Lomoz (ETD)
WASP-55	2456827.55355	0.00023	92.0	0.00002	This work (Danish)
WASP-55	2457135.68202	0.00019	161.0	0.00009	This work (Danish)

2007; Baraffe et al. 2008). Fig. 10 compares the positions of the four planets in the mass–radius diagram to the overall sample of planets¹⁰ and to predictions from Bodenheimer et al. (2003) for

¹⁰ Data on planetary systems were taken from TEPcat on 2015/11/09. Figs. 10 and 11 show only those planets regarded as “well-studied”, i.e. excluding planets which have been characterised as part of a large sample of planetary systems without receiving significant individual attention.

planetary equilibrium temperatures similar to those for the four planets which are the subject of the current work. Whilst WASP-22 b is well represented by models without a heavy-element core, the other three planets are significantly larger than predicted even for coreless gas giants. For comparison, Fig. 11 shows the same mass–radius diagram but with the predictions of the Baraffe et al. (2008) theoretical models for a range of heavy-element mass fractions, Z . All four planets are larger than model predictions even

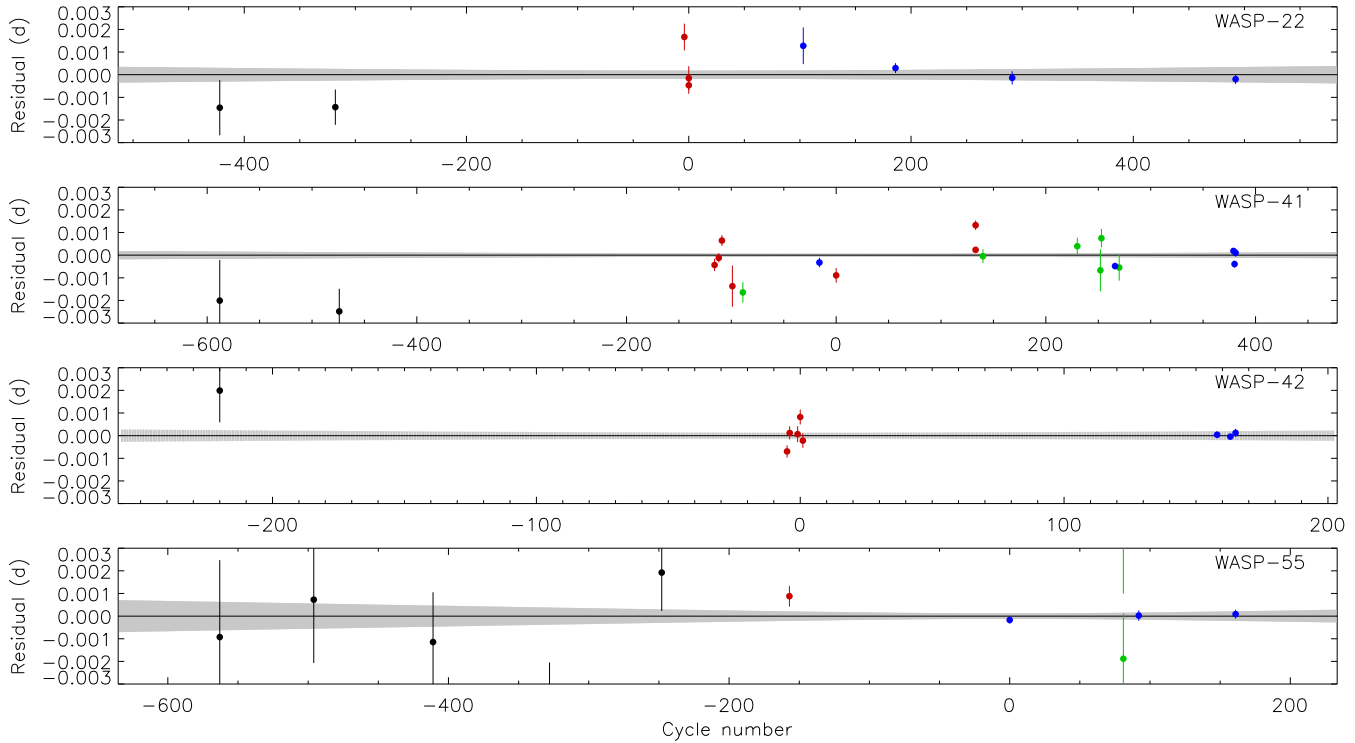


Figure 9. Plot of the residuals of the timings of mid-transit versus a linear ephemeris. The results from this work are shown in blue and from amateur observers in green. Our reanalysis of published data are shown in black for WASP-South observations and in red for other sources. The grey-shaded regions show the 1σ uncertainty in the ephemeris as a function of cycle number.

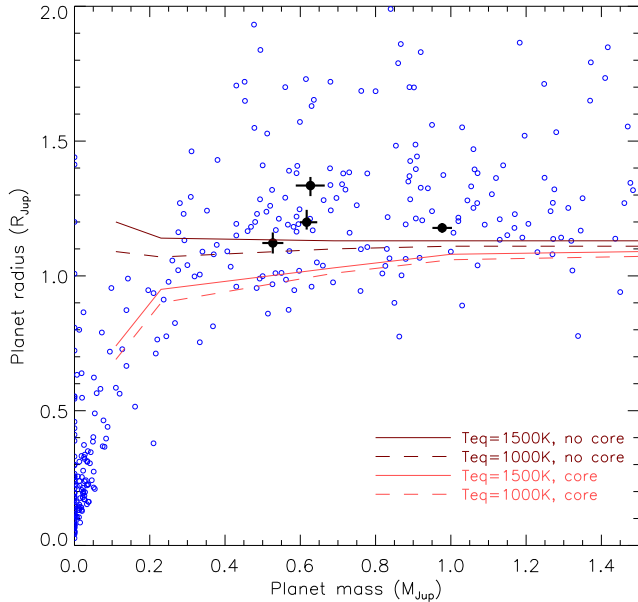


Figure 10. Plot of planet radii versus their masses. WASP-22 b, WASP-41 b, WASP-42 b and WASP-55 b are indicated using black filled circles. The overall population of planets is shown using blue open circles without errorbars, using data taken from TEPcat on 2015/11/09. The lines show the predicted planet radii of gas-giants from Bodenheimer et al. (2003, their table 1) for two different equilibrium temperatures (1000 K and 1500 K) which bracket the four planets, and for with and without a solid $20 M_{\oplus}$ core (see key).

for $Z = 0.02$, which yields the largest planetary radii of all the model sets. It is clear that all four planets are more inflated than expected, particularly WASP-55, and are therefore good candidates for the characterisation of their atmospheres via transmission spectroscopy and photometry (e.g. Nikolov et al. 2014; Mallonn et al. 2015).

Two of our transit light curves of WASP-41 show clear evidence for spot activity, with one spot crossing event observed on 2015/05/13 and two on 2015/05/17. We make the assumption that the spot observed on 2015/05/13 is the same as the second spot observed on 2015/05/17, as the measured spot radii and contrasts agree, and the resulting stellar rotation period and velocity are highly consistent with previous measurements obtained using different methods. The change in longitude of the spot then gives a stellar rotation period of 18.6 ± 1.5 d and $v \sin i$ of 2.4 ± 0.2 km s $^{-1}$, both at a latitude of approximately 12° . The change in latitude yields a measurement of the sky-projected orbital obliquity of the system of $\lambda = 6 \pm 11^\circ$, which is significantly more precise than a previous measurement obtained via the Rossiter-McLaughlin effect.

Spectroscopic measurements of λ are notoriously difficult for cool stars because the amplitude of the Rossiter-McLaughlin effect depends on the $v \sin i$ of the host star, which is typically very low below T_{eff} values of roughly 5500 K. Starspot tracking is a major contributor in this domain, with a total of ten determinations to date (Table 8 and Fig. 12). The host stars have T_{eff} values between 4645 K and 5576 K, so are all cool stars where Rossiter-McLaughlin measurements are difficult (e.g. Albrecht et al. 2011) but stars often show strong spot activity. The orbital obliquity of systems containing cool stars is a useful probe of tidal theory (e.g. Esposito et al. 2014; Mancini et al. 2015), and a statistically signif-

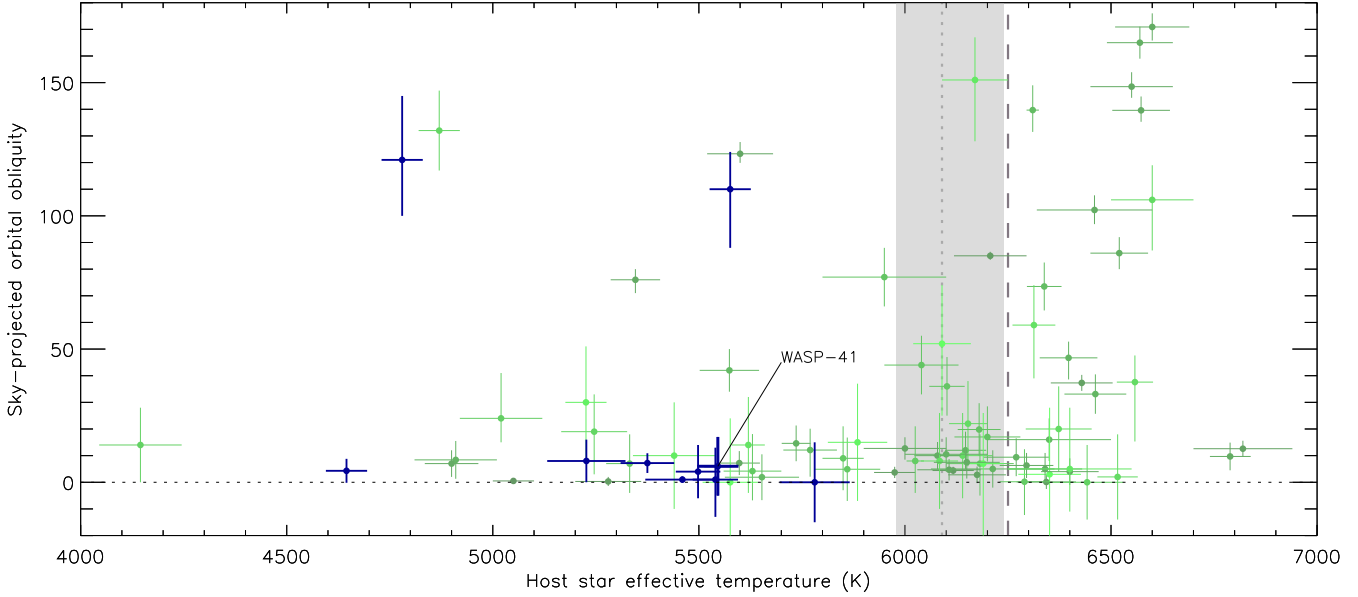


Figure 12. Plot of the sky-projected orbital obliquity angle λ versus the T_{eff} of the host star. The data come from TEPcat, obtained on 2015/11/09, and only the best value for each planetary system is plotted. Green lines show the measurements, graded for clarity from dark to light green depending on the size of the errorbars. Measurements obtained from spot tracking are shown with thicker blue lines. The T_{eff} values proposed as boundaries are shown using a grey dashed line (6250 K; Winn et al. 2010) and a grey shaded region with a dotted line to indicate the value and its uncertainties (6090 $^{+150}_{-110}$ K; Dawson 2014). Published values of λ have been adjusted by $\pm 180^\circ$ to bring them into the interval $[0^\circ, 180^\circ]$ (see Crida & Batygin 2014).

Table 8. Published measurements of the sky-projected, λ , and true, ψ , orbital obliquities obtained from spot-tracking analyses.

System	Host star T_{eff} (K)	λ ($^\circ$)	ψ ($^\circ$)	Reference
HAT-P-11	4780 \pm 50	105 $^{+16}_{-12}$ or 121 $^{+24}_{-21}$	106 $^{+15}_{-11}$ or 97 $^{+8}_{-4}$	Sanchis-Ojeda & Winn (2011)
HATS-02	5227 \pm 95	8 \pm 8		Mohler-Fischer et al. (2013)
Kepler-17	5781 \pm 85	0 \pm 15		Désert et al. (2011)
Kepler-30	5498 \pm 54	-1 \pm 10 or 4 \pm 10		Sanchis-Ojeda et al. (2012)
Kepler-63	5576 \pm 50	-110 $^{+22}_{-14}$	145 $^{+9}_{-14}$	Sanchis-Ojeda et al. (2013)
Qatar-2	4645 \pm 50	4.3 \pm 4.5		Mancini et al. (2014)
WASP-4	5540 \pm 55	-1 $^{+14}_{-12}$		Sanchis-Ojeda et al. (2011)
WASP-6	5375 \pm 65	7.2 \pm 3.7		Tregloan-Reed et al. (2015)
WASP-19	5460 \pm 90	1.0 \pm 1.2		Tregloan-Reed et al. (2013)
WASP-41	5546 \pm 33	6 \pm 11		This work

icant sample of such measurements is both scientifically important and observationally tractable via starspot tracking analyses such as that performed for WASP-41.

ACKNOWLEDGEMENTS

The operation of the Danish 1.54m telescope is financed by a grant to UGJ from the Danish Council for Independent Research, Natural Sciences (FNU). The reduced light curves presented in this work will be made available at the CDS (<http://vizier.u-strasbg.fr/>) and at <http://www.astro.keele.ac.uk/jkt/>. We thank Laetitia Delrez and Marion Neveu-VanMalle for providing published light curves of WASP-41. J.Southworth acknowledges financial support from the Leverhulme Trust in the form of a Philip Leverhulme Prize. JTR acknowledges financial support from ORAU (Oak Ridge Associated Universities) and NASA in the form of a NASA Post-Doctoral Programme (NPP) Fellowship. DFE is

funded by the UK's Science and Technology Facilities Council. EU-S acknowledges the support of CONICYT QUIMAL 130004 project. Funding for the Stellar Astrophysics Centre in Aarhus is provided by The Danish National Research Foundation (grant agreement no. DNR106). The research is supported by the ASTERISK project (ASTERoseismic Investigations with SONG and Kepler) funded by the European Research Council (grant agreement no. 267864). TCH acknowledges KASI research grants #2012-1-410-02, #2013-9-400-00, #2014-1-400-06 and #2015-1-850-04. NP acknowledges funding by the Gemini-Conicyt Fund, allocated to project No. 32120036. GD acknowledges Regione Campania for support from POR-FSE Campania 2014–2020. YD, AE, OW and JSurdej acknowledge support from the Communauté française de Belgique - Actions de recherche concertées - Académie Wallonie-Europe. The following internet-based resources were used in research for this paper: the ESO Digitized Sky Survey; the NASA Astrophysics Data System; the SIMBAD database and VizieR catalogue access tool operated at CDS,

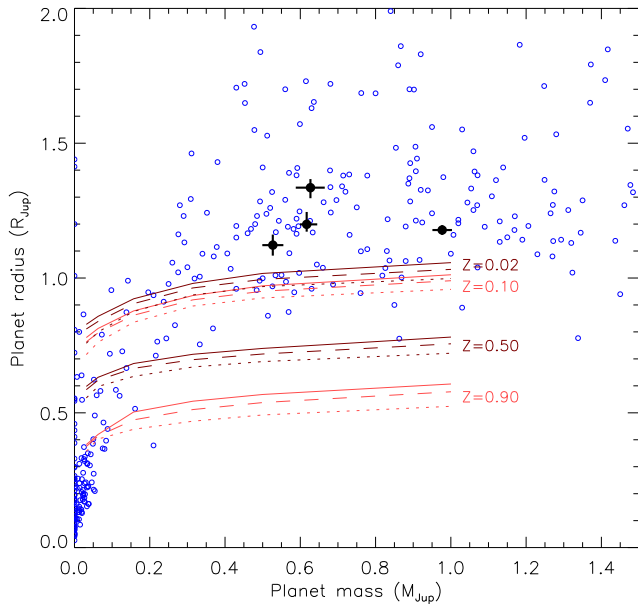


Figure 11. As Fig. 10 but with different theoretical predictions. The lines show the predicted planet radii of gas-giants from Baraffe et al. (2008, their table 4) for four different heavy-element mass fractions Z , labelled on the plot. The unbroken lines show predictions for a planet of age 0.5 Gyr, the dashed lines for an age of 1 Gyr and the dotted lines for an age of 5 Gyr. The lines are colour-coded for clarity.

Strasbourg, France; and the arXiv scientific paper preprint service operated by Cornell University.

REFERENCES

- Albrecht, S., et al., 2011, *ApJ*, 738, 50
 Anderson, D. R., et al., 2011, *A&A*, 534, A16
 Baraffe, I., Chabrier, G., Barman, T., 2008, *A&A*, 482, 315
 Barros, S. C. C., Boué, G., Gibson, N. P., Pollacco, D. L., Santerne, A., Keenan, F. P., Skillen, I., Street, R. A., 2013, *MNRAS*, 430, 3032
 Bodenheimer, P., Laughlin, G., Lin, D. N. C., 2003, *ApJ*, 592, 555
 Carter, J. A., Yee, J. C., Eastman, J., Gaudi, B. S., Winn, J. N., 2008, *ApJ*, 689, 499
 Claret, A., 2004, *A&A*, 424, 919
 Crida, A., Batygin, K., 2014, *A&A*, 567, A42
 Dawson, R. I., 2014, *ApJ*, 790, L31
 Demarque, P., Woo, J.-H., Kim, Y.-C., Yi, S. K., 2004, *ApJS*, 155, 667
 Désert, J.-M., et al., 2011, *ApJS*, 197, 14
 Dotter, A., Chaboyer, B., Jevremović, D., Kostov, V., Baron, E., Ferguson, J. W., 2008, *ApJS*, 178, 89
 Eastman, J., Siverd, R., Gaudi, B. S., 2010, *PASP*, 122, 935
 Eaton, N., Draper, P. W., Allen, A., 1999, *Starlink User Note* 45.9
 Esposito, M., et al., 2014, *A&A*, 564, L13
 Evans, D. F., et al., 2015, *A&A*, submitted
 Fortney, J. J., Marley, M. S., Barnes, J. W., 2007, *ApJ*, 659, 1661
 Gibson, N. P., et al., 2009, *ApJ*, 700, 1078
 Hellier, C., et al., 2012, *MNRAS*, 426, 739
 Howell, S. B., et al., 2014, *PASP*, 126, 398
 Ioannidis, P., Huber, K. F., Schmitt, J. H. M. M., 2016, *A&A*, 558, A72
 Jehin, E., et al., 2011, *The Messenger*, 145, 2
 Knutson, H. A., et al., 2014, *ApJ*, 785, 126
 Lendl, M., et al., 2012, *A&A*, 544, A72
 Lucy, L. B., Sweeney, M. A., 1971, *AJ*, 76, 544
 Mallonn, M., et al., 2015, *A&A*, 580, A60
 Mancini, L., et al., 2014, *MNRAS*, 443, 2391
 Mancini, L., et al., 2015, *A&A*, 579, A136
 Maxted, P. F. L., Koen, C., Smalley, B., 2011a, *MNRAS*, 418, 1039
 Maxted, P. F. L., et al., 2010, *AJ*, 140, 2007
 Maxted, P. F. L., et al., 2011b, *PASP*, 123, 547
 Mohler-Fischer, M., et al., 2013, *A&A*, 558, A55
 Mortier, A., Santos, N. C., Sousa, S. G., Fernandes, J. M., Adibekyan, V. Z., Delgado Mena, E., Montalto, M., Israelian, G., 2013, *A&A*, 558, A106
 Neveu-VanMalle, M., et al., 2015, *A&A*, in press, arXiv:1509.07750
 Nikolov, N., et al., 2014, *MNRAS*, 437, 46
 Nutzman, P. A., Fabrycky, D. C., Fortney, J. J., 2011, *ApJ*, 740, L10
 Oshagh, M., Santos, N. C., Boisse, I., Boué, G., Montalto, M., Dumusque, X., Haghighipour, N., 2013, *A&A*, 556, A19
 Pietrinferni, A., Cassisi, S., Salaris, M., Castelli, F., 2004, *ApJ*, 612, 168
 Poddaný, S., Brát, L., Pejcha, O., 2010, *New Astronomy*, 15, 297
 Pollacco, D. L., et al., 2006, *PASP*, 118, 1407
 Pont, F., Husnoo, N., Mazeh, T., Fabrycky, D., 2011, *MNRAS*, 414, 1278
 Sanchis-Ojeda, R., Winn, J. N., 2011, *ApJ*, 743, 61
 Sanchis-Ojeda, R., Winn, J. N., Holman, M. J., Carter, J. A., Osip, D. J., Fuentes, C. I., 2011, *ApJ*, 733, 127
 Sanchis-Ojeda, R., et al., 2012, *Nature*, 487, 449
 Sanchis-Ojeda, R., et al., 2013, *ApJ*, 775, 54
 Silva-Valio, A., 2008, *ApJ*, 683, L179
 Skottfelt, J., et al., 2015, *A&A*, 574, A54
 Southworth, J., 2008, *MNRAS*, 386, 1644
 Southworth, J., 2009, *MNRAS*, 394, 272
 Southworth, J., 2011, *MNRAS*, 417, 2166
 Southworth, J., 2012, *MNRAS*, 426, 1291
 Southworth, J., 2013, *A&A*, 557, A119
 Southworth, J., et al., 2009, *MNRAS*, 396, 1023
 Southworth, J., et al., 2014, *MNRAS*, 444, 776
 Stetson, P. B., 1987, *PASP*, 99, 191
 Ter Braak, C. J. F., 2006, *Statistics and Computing*, 16, 239
 Tregloan-Reed, J., Southworth, J., Tappert, C., 2013, *MNRAS*, 428, 3671
 Tregloan-Reed, J., et al., 2015, *MNRAS*, 450, 1760
 VandenBerg, D. A., Bergbusch, P. A., Dowler, P. D., 2006, *ApJS*, 162, 375
 Winn, J. N., Fabrycky, D., Albrecht, S., Johnson, J. A., 2010, *ApJ*, 718, L145